Large Magnetoresistance and Perfect Spin-Injection Efficiency in Two-Dimensional Strained VSi$_2$N$_4$-Based Room-Temperature Magnetic-Tunnel-Junction Devices

Guohui Zhan[,1,2] Zhilong Yang,[3] Kun Luo,[1] Shengli Zhang,[4,*] and Zhenhua Wu[1,2,†]

[1]*Institute of Microelectronics, Chinese Academy of Sciences, Beijing 100029, China*

[2]*University of Chinese Academy of Sciences, Beijing 100049, China*

[3]*National Laboratory of Solid State Microstructures, School of Physics, Nanjing University, Nanjing 210093, China*

[4]*Key Laboratory of Advanced Display Materials and Devices, College of Material Science and Engineering, Nanjing University of Science and Technology, Nanjing 210094, China*

Two-dimensional (2D) materials provide a promising platform for exploring spintronic devices. However, the low Curie temperature of most 2D magnetic materials limits their development and application. Based on density-functional theory and the nonequilibrium-Green's-function formalism, we present a systematic simulation study of room-temperature strained VSi$_2$N$_4$-based magnetic tunnel junctions (MTJs), using a high-accuracy Heyd-Scuseria-Ernzerhof (HSE) functional. In contrast to Perdew-Burke-Ernzerhof results, a spin-conductance match is observed in Ag/VSi$_2$N$_4$-VSi$_2$N$_4$/Ag MTJs at the HSE06 level. Thus, a 1200% tunnel-magnetoresistance (TMR) ratio and a perfect spin-injection efficiency are theoretically predicted in Ag/VSi$_2$N$_4$-VSi$_2$N$_4$/Ag MTJs. Interestingly, the coexistence of a Weyl semimetal and a half-metal state is found in 1.965% tensile-biaxial-strained monolayer VSi$_2$N$_4$. In addition, a slight compressive strain leads to a boost of the TMR ratio by 2 orders of magnitude, up to 10^5% in strained VSi$_2$N$_4$-based MTJs. Other MTJs based on VSi$_2$P$_4$, VSi$_2$As$_4$, and NbSi$_2$N$_4$ are investigated. Our results show that these spin-polarized magnetic silicide compounds, with Curie temperatures close to room temperature, are promising candidates for next-generation spintronic devices.

I. INTRODUCTION

Being widely used devices in spintronics, magnetic tunnel junctions (MTJs) have attracted wide interest for their promising and successful application, such as in magnetic sensors and magnetoresistive random access memory devices. For decades, a lot of effort has been devoted to improving device performance [1–7], from the early Al$_2$O$_3$-based MTJs to crystalline MgO-based MTJs and MTJs based on various other materials. There are some important metrics for designing MTJ devices: (1) The *tunnel magnetoresistance* (TMR): a higher value indicates a better switching effect. For example, a large TMR of 604% has been achieved in MgO-based MTJ devices [7]. (2) The *Curie temperature* (T_C): a high T_C ensures that the device can work at room temperature. (3) The *magnetic anisotropy energy* (MAE), which is related to the thermal stability of the device, i.e., the stability of the magnetic

moment against thermal disturbance [8]. Therefore, developing MTJ devices with a high T_C, a high TMR, and a sufficiently large MAE is a key point for next-generation spintronic devices.

There is a demand for the scaling down of devices, but it is difficult to scale three-dimensional materials for use in future high-density spintronic devices. Two-dimensional (2D) materials offer a broader platform, with the natural advantage of being ultrathin on the atomic scale. Since 2017, a large number of 2D magnetic materials have been experimentally discovered, such as Cr$_2$Ge$_2$Te$_6$ [9], CrI$_3$ [10], and Fe$_3$GeTe$_2$ [11]. Some of these have been theoretically predicted and experimentally verified to be good candidates for future 2D MTJs [12–18]. For example, Fe$_3$GeTe$_2$-based MTJs can achieve a TMR ratio of over 1000%, and monolayer Fe$_3$GeTe$_2$ exhibits large out-of-plane MAE values (about 0.8 meV/atom) [19,20]. However, most of the current 2D magnetic materials have a very low Curie temperature; for example, the T_C values of Fe$_3$GeTe$_2$ and CrI$_3$ are close to 100 and 50 K, respectively. To some extent, these low Curie temperatures limit the development and application of 2D MTJs.

_____

*zhangslvip@njust.edu.cn

†wuzhenhua@ime.ac.cn

Recently, two-dimensional $MoSi_2N_4$ materials were successfully grown by chemical vapor deposition [21]; the family of MA_2Z_4 ($M = $ Mo, W, V, Nb; $A = $ Si, Ge; $Z = $ N, P, As) monolayers immediately attracted widespread research attention due to its excellent physical properties [22–30]. Wang *et al.* have predicted nine thermodynamically and dynamically stable ferromagnetic systems [23]. Among them, the silicide compounds (VSi_2N_4, VSi_2P_4, VSi_2As_4, and $NbSi_2N_4$) are more stable than the germanide compounds from the formation enthalpies, and Perdew-Burke-Ernzerhof (PBE)-calculated results show that these magnetic materials have half-metallic behaviors. More importantly, the T_C values of these materials are predicted to be close to room temperature. Therefore, they may be good candidates for designing scaled MTJ devices.

Previous work has focused mainly on the electronic states and magnetic properties of monolayer MA_2Z_4. Here, we specifically investigate the spin-dependent transport properties and possible device application of these magnetic silicide compounds, and the more accurate Heyd-Scuseria-Ernzerhof (HSE) HSE06 functional is used in the transport simulations. In Sec. III A, we study the basic electronic states of monolayer VSi_2N_4 with PBE and HSE06 levels. The accurate HSE06 band structure under 1.965% strain reveals that the spin-up band shows a strong signature of Weyl semimetallic behavior. It is also found that the in-plane easy axis can be changed to an out-of-plane easy axis by a tensile strain. In Sec. III B, the spin-dependent transport properties of Ag/VSi_2N_4-VSi_2N_4/Ag MTJs are theoretically investigated, and a large TMR ratio of 1200% and perfect spin-injection efficiency are predicted. Surprisingly, the TMR ratio can be increased by up to 10^5% by a compressive biaxial strain, as shown in Sec. III C. In Sec. III D, it is found that VSi_2N_4-based MTJs with vacuum barriers have better performance than those using the graphene, *h*-BN, and $MoSi_2N_4$ layers. Finally, we also consider three other silicide compounds, and a similar TMR ratio can be found in VSi_2As_4-based MTJ devices.

II. COMPUTATIONAL METHODS

In our simulations, all of the geometry optimization of bulk materials, interfaces, and MTJ devices is performed by using the Vienna *ab initio* simulation program (VASP) based on density-functional theory [31]. The exchange-correlation interaction is described by a generalized gradient approximation (GGA) with a Hubbard-U-parameter (GGA + U = 3 eV) approach in the form of a PBE potential. The crystal structures are optimized until the energy difference is less than 10^{-7} eV. The DFT-D2 method is used to describe the weak van der Waals (vdW) interaction.

The electronic properties and quantum transport properties are obtained by using density-functional theory (DFT)

combined with the nonequilibrium-Green's-function formalism, as implemented in QuantumATK [32]. It should be noted that the PBE functional often underestimates the band gap, and the HSE06 functional for the spin-polarized generalized gradient approximation to the exchange-correlation potential is also employed in all simulations [33]. The dynamical stability is verified from phonon calculations using a $5 \times 5 \times 1$ supercell. For MAE calculations, the effect of spin-orbit coupling (SOC) must be included; the noncollinear spin-orbit GGA is adapted for use in the SOC calculations. Note that the MAE value is very small, and $21 \times 21 \times 1$ k-point meshes are large enough for complete convergence. For quantum transport calculations, the real-space mesh cutoff is taken as 150 hartree, and $11 \times 11 \times 151$ k-point meshes are used for self-consistent calculations of the electrode region and the central region. When a bias voltage is applied, the current I_σ passing through the device is calculated from the Landauer-Buttiker formula,

$$I_\sigma = \frac{2e}{h} \int T_\sigma(E,V)[f_L(E - eV/2) - f_R(E + eV/2)]\, dE \tag{1}$$

where $T_\sigma(E, V)$ is the transmission spectrum, σ is the spin label, and f_L and f_R are the Fermi-Dirac distributions of the left and right electrodes, respectively.

III. RESULTS AND DISCUSSION

A. Electronic properties of monolayer VSi_2N_4

Figure 1(a) shows the crystal structure of the 2D monolayer VSi_2N_4, which consists of a septuple layer N-Si-N-V-N-Si-N arranged along the z direction. The optimized lattice constant is $a = b = 2.88$ Å. The crystal is described by the point group D_{3h}, where the inversion symmetry is broken but mirror symmetry is retained. To confirm the stability of the monolayer, we calculate the phonon band structure, as shown in Fig. 1(c), where the absence of an imaginary frequency mode reveals that the crystal structure is dynamically stable. Subsequently, we investigate the electronic states of monolayer VSi_2N_4 with PBE and HSE06 levels. First-principles calculations show that the monolayer has an in-plane magnetization, and the magnetic moment of the V atom is about $0.9\mu_B$. (More details can be found in Fig. S1 in the Supplemental Material [34].) From Fig. 1(d), the monolayer is a ferromagnetic metal according to the PBE functional. However, the more accurate HSE06 results show that the monolayer VSi_2N_4 is a magnetic semiconductor rather than a metal, and the direct band gap is around 0.5 eV. It is worth mentioning that there exists an almost fully spin-polarized band around the Fermi energy according to the results for the two functionals.
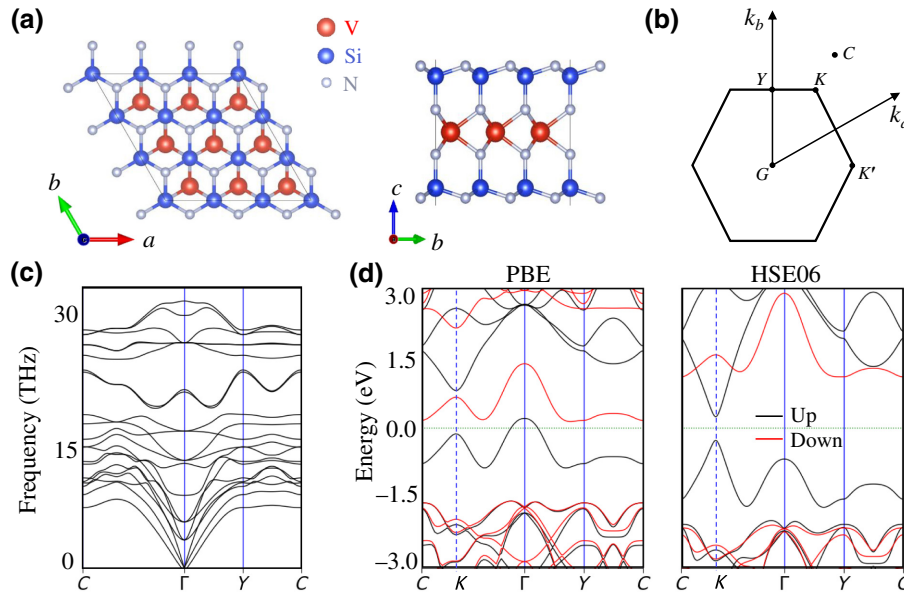
FIG. 1. (a) Top and side views of crystal structure of VSi_2N_4. (b) High-symmetry points in 2D Brillouin zone. (c) Phonon spectrum of monolayer VSi_2N_4. (d) Band structure of monolayer VSi_2N_4 with PBE and HSE06 levels; the black and red lines denote spin up and spin down, respectively.

Uniaxial and biaxial strains are often spontaneously induced due to lattice mismatch around the interface during the growth of materials on substrates. To explore the effect of strain, an in-plane biaxial strain is applied to the monolayer VSi_2N_4 . The biaxial strain coefficient is defined as $\varepsilon = (a - a_0)/a_0$, where a_0 and a are the original and deformed lattice constants, respectively. Figure 2(a) shows the band structure without the SOC effect under a biaxial strain from -3% to 3%, and the phonon spectrum shows that it is still dynamically stable under slight strains (see Fig. S4 in the Supplemental Material [34]). As the compressive strain increases, the band gap becomes larger. When a tensile strain is applied, the monolayer undergoes several different transitions: the band gap is gradually reduced to zero and then reopens. More specifically, a critical gapless band crossing is induced by 1.965% tensile strain, resulting in a linear cone located at the K and K' point around the Fermi energy [See Fig. 2(b)]. Noted that the state under 1.965% tensile strain is both a Weyl semimetal and a half-metal. Furthermore, we calculate the partial orbital density of this state and find that it consists of mainly a d-orbital contribution of V atoms around the Fermi energy, and that the three orbitals of the V atom are d_{xy}, $d_{x^2-y^2}$, and d_{z^2}. Similarly to Ref. [35,36], the effective model around $K(K')$ has the form $H(q) = v_F(\tau q_x \sigma_x + q_y \sigma_y)$, where v_F is the Fermi velocity, and $\tau = \pm 1$ for the K or K' point. The effective v_F of the Weyl cones is calculated to be around 3.0×10^6 m/s, which is 3 times larger than for graphene, suggesting that monolayer VSi_2N_4 may have great potential application in high-speed electronic devices.

It is known that large MAE values are essential for the thermal stability of MTJ devices. We calculate the total energy of VSi_2N_4 in the presence of spin-orbit coupling at the HSE06 level with different magnetic configurations, oriented towards in-plane (100) and out-of-plane (001) directions. The MAE value is defined as $E_{001} - E_{100}$. The MAE under different biaxial strains is shown in Fig. 2(c); the value of 0.01 meV/atom for the undeformed structure indicates that an in-plane magnetization is favored. More interestingly, the magnetic ground state of the monolayer can be changed by the biaxial strain. When a compressive strain is applied, the monolayer exhibits a larger MAE; the MAE value is near 0.10 meV/atom at -4% strain and is larger than those for the common ferromagnets Fe and Co [20]. Our calculations show that the very small MAE value of the monolayer can be increased by biaxial strain.

B. Spin-dependent transport properties

To evaluate the characteristics of the VSi_2N_4-based MTJ device based on its spin-polarized subband near the Fermi level, the spin-dependent transport properties are calculated. As shown in Fig. 3, metallic Ag is one of the most commonly used electrodes in device experiments, and the Ag(111) surface ($a = b = 2.88$ Å) is perfectly matched with this magnetic material. Therefore, a two-dimensional vdW MTJ device is easily constructed, namely a Ag/VSi_2N_4-VSi_2N_4/Ag model, in which the vacuum is viewed as tunnel barriers [Fig. 3(a)]. The optimum distances of the Ag-N and N-N bonds are 2.68 and 3.33 Å, respectively. The state with the magnetic moments
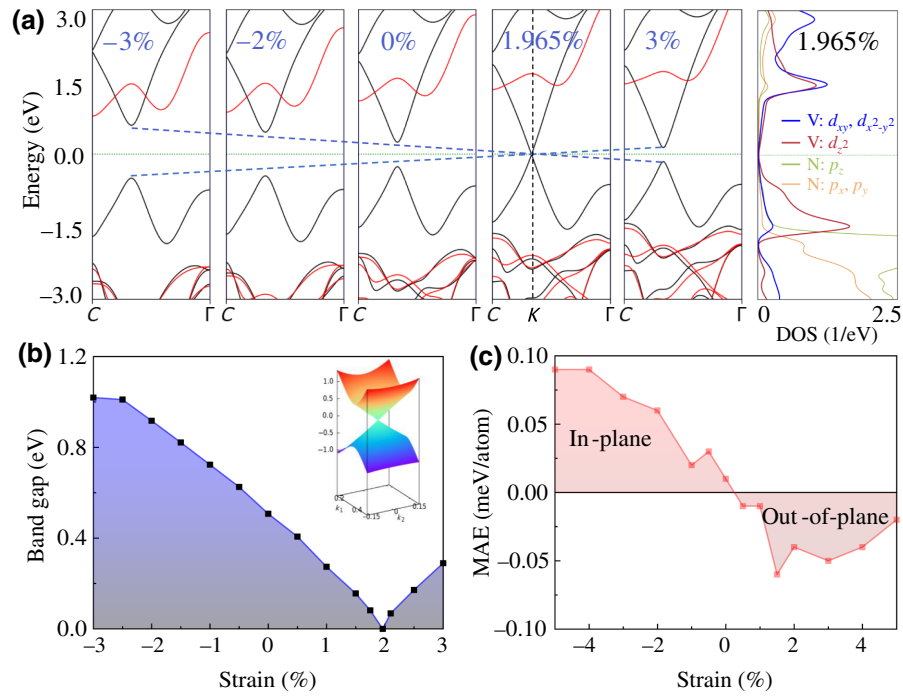
FIG. 2.   (a) Band structure of monolayer VSi_2N_4 under different biaxial strains, and partial orbital density of states under 1.965% strain. (b) Band gap as a function of biaxial strain; the inset shows the gapless Weyl cone. (c) MAE values as a function of biaxial strain. The HSE06 functional is used in these calculations.

of the V atoms arranged in a parallel (antiparallel) manner is defined as the *P* (AP) configuration. By an externally induced method, the *P* configuration can be transferred to the AP configuration, bringing about a switching of low and high resistance. There is no obvious difference between the bands with and without the SOC effect, and so this effect is ignored in the present work.

Here, for comparison, we present the quantum transport results calculated by use of the two functionals, that is, the PBE and HSE06 levels. For the PBE-calculated result, the maximum current (40 nA) in the *P* configuration is much larger than that for the HSE06 level [Figs. 3(b) and 3(d)]. This is due to the large density of states (DOS) near the Fermi level in the PBE-calculated band structure. It is worth noting that the spin-down current is larger than the current in the spin-up channel [Fig. 3(d)] because the bands of the magnetic material are shifted down after the metal and semiconductor are placed in contact.

Moreover, the current in Fig. 3(b) rapidly decreases when the bias is larger than 0.1 V, showing a typical negative-differential-resistance effect. However, the results of the HSE06 calculation are obviously different. We introduce the spin-injection efficiency (SIE), *S*, as follows:

$$S = \left| \frac{I_{up} - I_{down}}{I_{up} + I_{down}} \right|. \tag{2}$$

If a large spin polarization does not exist in the material, then I_{up} and I_{down} are the same and the SIE is near zero. Based on our calculations, it is found that the SIE is only near 60% according to the PBE level, but there exists a perfect spin-filtering ratio in the *P* configuration according to the HSE06 functional [Fig. 3(d)]. To obtain a better understanding of the spin-injection efficiency, an equivalent schematic illustration is presented in Fig. 4, where the spin-up and spin-down channels form a parallel connection of resistances, including the resistance of the metallic Ag, the VSi_2N_4, and different barriers (such as the vacuum and insulators). So, Eq. (2) can also be written as

$$S = \left| \frac{R_{down} - R_{up}}{R_{down} + R_{up}} \right| = \left| \frac{R'_{VSi_2N_4,down} - R'_{VSi_2N_4,up}}{R_{Ag} + R'_{VSi_2N_4}} \right|, \tag{3}$$

where R_{Ag} stands for the resistance of the Ag, and $R'_{VSi_2N_4}$ denotes the total resistance of the VSi_2N_4 and the barriers. According to the HSE06-calculated result in the *P* configuration [Fig. 3(d)], it can be deduced that $R_{Ag} \ll R'_{VSi_2N_4}$ and $R'_{VSi_2N_4,up} \gg R'_{VSi_2N_4,down}$, indicating a perfect spin-conductance match [37,38].

The TMR ratio is a key value for MTJ devices, and its value is defined as

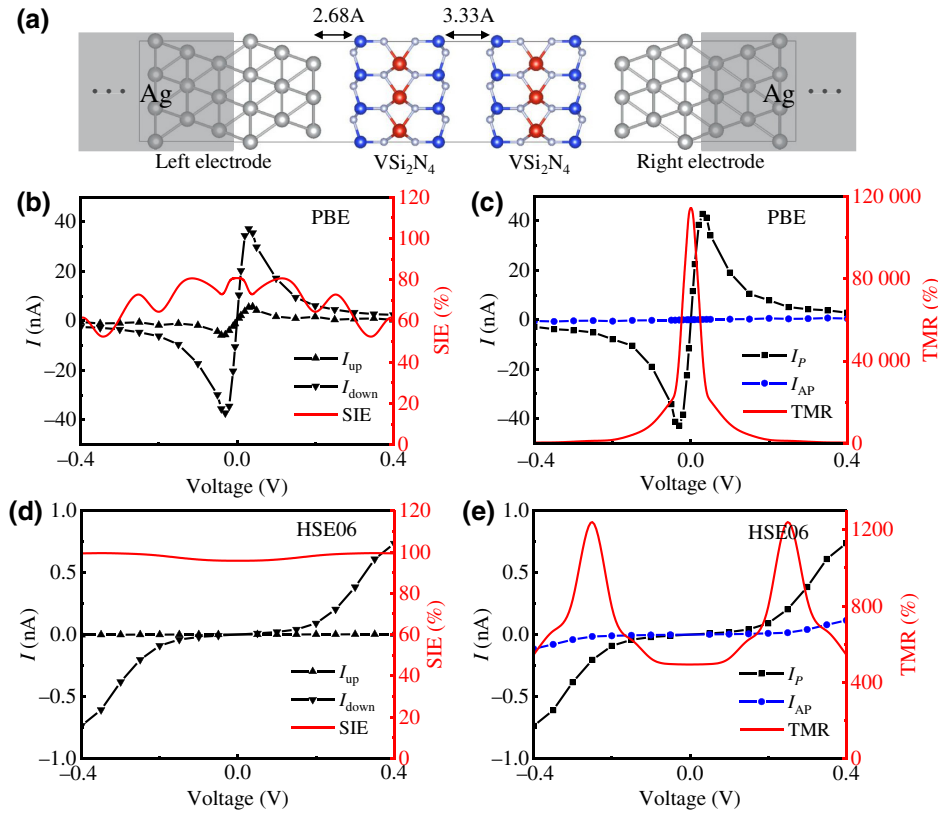$$\frac{R_{AP} - R_P}{R_P} = \frac{I_P - I_{AP}}{I_{AP}}, \tag{4}$$

FIG. 3. (a) Model of the $Ag/VSi_2N_4-VSi_2N_4/Ag$ device, where metallic Ag is used as the left and right electrodes. (b),(d) Spin-dependent current (I_{up}, I_{down}) and spin-injection efficiency in the P configuration with PBE (b) and HSE06 (d) levels. (c),(e) I-V characteristics of P and AP configurations and TMR ratio with PBE (c) and HSE06 (e) levels.

where I_P and I_{AP} are the total currents in the P and AP configurations, respectively. As shown in Figs. 3(c) and 3(e), the PBE-calculated results show a giant tunnel magnetoresistance and a large switching ability, which is similar to that of a planar $MoSi_2N_4/VSi_2N_4-VSi_2N_4/MoSi_2N_4$ MTJ [30]. But the HSE06 calculations provide more accurate and realistic results: the maximum TMR ratio is only 1200% at 0.25 eV, and the value is 6 times larger than that for the well-known Fe/MgO/Fe MTJs [4]. Additionally, planar devices are not easy to fabricate experimentally, and handling the dangling surface is still challenging. Therefore, VSi_2N_4-based devices with vdW materials connected are expected to be future possible 2D MTJ devices.

C. Effect of strain on MTJ devices

Strain engineering is an effective and useful tool in most device experiments. To explore the effect of strain on the MTJ devices, the spin-dependent transport properties under different biaxial strains from -4% to 2% are investigated by high-accuracy HSE06 calculations. Figure 5(a) shows the I-V characteristics under biaxial strain. It is found that a tensile strain decreases the TMR ratio, while a compressive biaxial strain effectively improves the TMR ratio of a $Ag/(\varepsilon\text{-}VSi_2N_4)-(\varepsilon\text{-}VSi_2N_4)/Ag$ MTJ. For example, applying a compressive biaxial strain $\varepsilon = -4\%$ can achieve a TMR ratio of approximately $10^5\%$. These results show that strain is a very important and effective control method that can greatly improve the device performance.

To obtain better insight into the effect of strain on strained VSi_2N_4-based MTJs, the transmission spectrum under -2% strain is also depicted in Fig. 5(b), where it is obvious that there is a huge difference in the transmission spectrum between the P and AP configurations. Further, we plot the spin-resolved projected local density of states (PLDOS) along the z direction in the P and AP
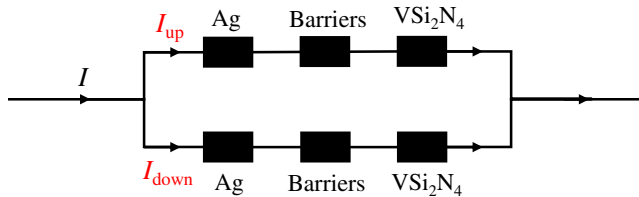

FIG. 4. Equivalent schematic illustration of a metal/ferromagnetic contact represented as a parallel connection of resistances. The top and bottom parts represent spin-up and spin-down polarized electrons, respectively.
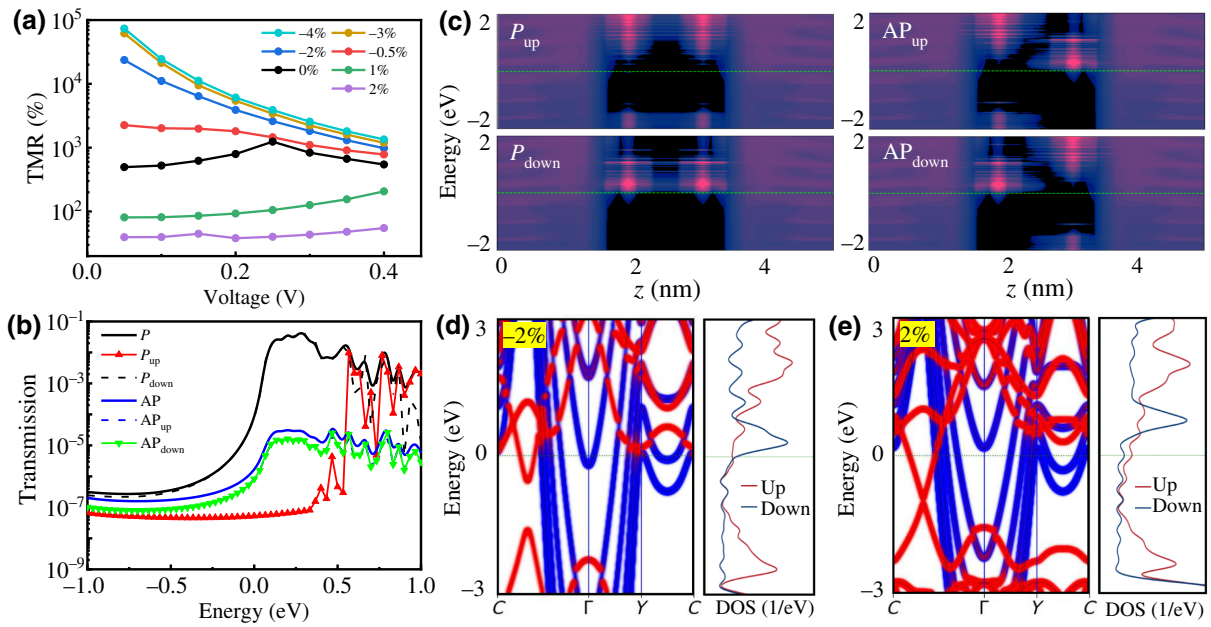
FIG. 5. (a) TMR ratio as a function of bias voltage under different strains. (b) Transmission spectra of P and AP configurations under -2% biaxial strain, where black and blue represent the total transmission of the P and AP configurations, respectively. (c) Spin-resolved PLDOS of P and AP configurations under -2% biaxial strain. (d),(e) Band structure and spin-resolved DOS of Ag-VSi$_2$N$_4$ junction under -2% (d) and 2% (e) strain, where blue and red denote the contributions from Ag and VSi$_2$N$_4$, respectively. The HSE06 level is used in these calculations.

configurations under -2% strain; there is a majority density of states for the spin-down channel, showing that the spin-down channel is of low resistance. In contrast, there is almost no density of states near the Fermi level for the spin-up channel, indicating that the spin-up channel is of high resistance. In addition, we calculate the projected band structure and DOS of the Ag/(ε-VSi$_2$N$_4$) heterojunction under compressive (-2%) and tensile (2%) strain to identify the effects of tensile and compressive strain on the magnetic material. As shown in Figs. 5(d) and 5(e), we find that the band of the VSi$_2$N$_4$ is shifted down due to the band alignment after contact, and when a compressive strain is applied, there is a large spin polarization near the Fermi level, while this is not the case when a tensile strain is applied. This is the origin of the large differences in the TMR of the strained VSi$_2$N$_4$-based MTJ device under different strains.

D. Different tunnel barriers

Usually, tunnel barriers between two ferromagnetic materials can modulate the TMR ratio in MTJ devices. For example, MgO-based MTJs have excellent performance, better than that of Al$_2$O$_3$-based MTJs. We choose some feasible layers with $X =$ (graphene, h-BN, MoSi$_2$N$_4$) in the present work, because graphene and h-BN are very common interfacial layers, and MoSi$_2$N$_4$ and VSi$_2$N$_4$ have similar crystal structures. As shown in Fig. 6(a), we design

Ag/VSi$_2$N$_4$-X-VSi$_2$N$_4$/Ag MTJ devices without strain. The I-V curves for the P and AP configurations are also shown in Fig. 6(b). It is found that the MTJs with $X =$ h-BN and MoSi$_2$N$_4$ have similar I-V characteristics, while the MTJ with $X =$ MoSi$_2$N$_4$ has a very small and weak current due to the higher tunnel barriers, and the MTJs with $X = h$-BN and graphene have current intensities close to each other. Figure 6(c) summarizes the fact that the TMR ratio in MTJs with vacuum barriers is larger than in the others and shows that the MTJ with graphene exhibits an oscillating behavior and an unstable current [39,40], indicating that Ag/VSi$_2$N$_4$-VSi$_2$N$_4$/Ag MTJs have better performance than that of devices using graphene, h-BN, and MoSi$_2$N$_4$ layers.

Without loss of generality, the spin-dependent transport properties of three other silicide compounds (VSi$_2$P$_4$, VSi$_2$As$_4$, and NbSi$_2$N$_4$) are investigated. These materials have similar structures, and the lattice constants of the three materials are 3.48, 3.64, and 2.96 Å, respectively. Some related papers have reported that the Curie temperatures of VSi$_2$P$_4$ and VSi$_2$As$_4$ are also close to room temperature [23,26]. Our quantum transport simulations show that similar performance and large TMR values are achieved in these MTJs. For example, a TMR ratio of about 1000% can achieved in VSi$_2$As$_4$-based MTJs (see Fig. S5 in the Supplemental Material [34]), which have a device performance the similar to that of VSi$_2$N$_4$-based devices. The TMR ratio versus the Curie temperature
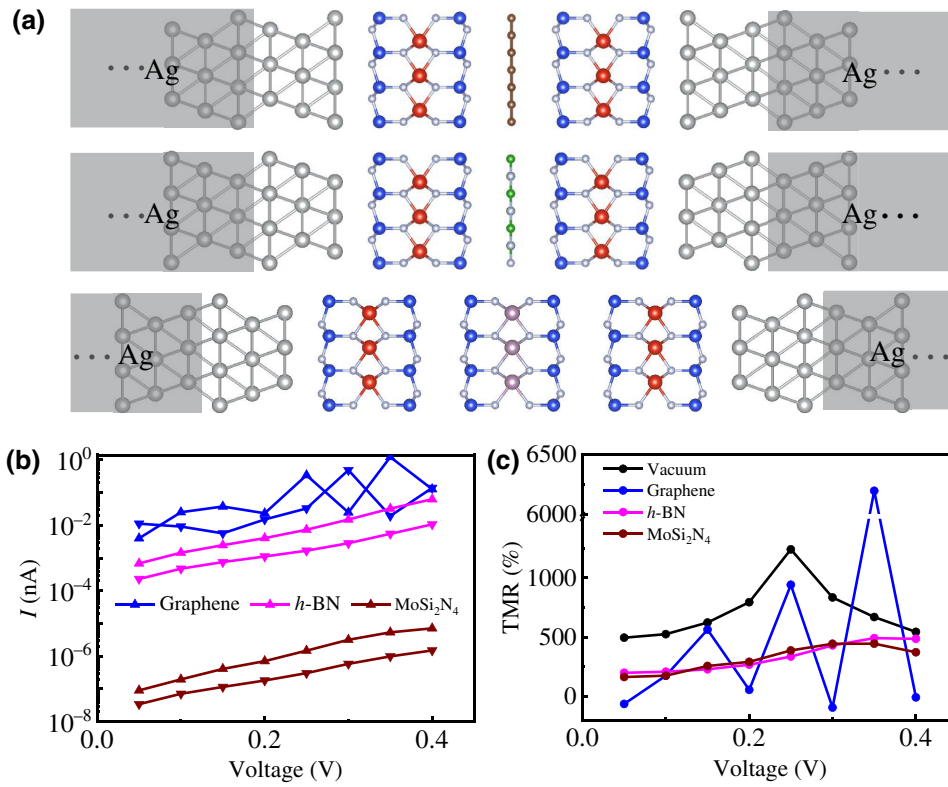
FIG. 6. (a) Device model of Ag/VSi_2N_4-X-VSi_2N_4/Ag structure using different tunnel barriers (X = graphene, h-BN, $MoSi_2N_4$). (b),(c) I-V characteristics (b) and TMR ratio (c) of Ag/VSi_2N_4-X-VSi_2N_4/Ag MTJ devices. The HSE06 level is used in these calculations.

(T_C) for two-dimensional-materials-based MTJs is benchmarked in Fig. 7. Although it is currently challenging to grow these magnetic materials experimentally, these results show that these magnetic silicide compounds with high T_C are promising candidates for 2D MTJs.
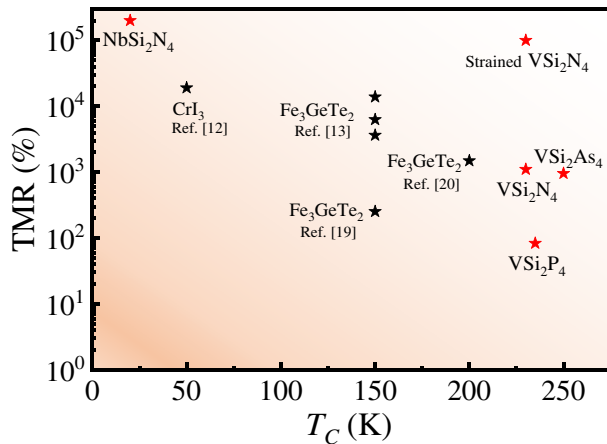
IV. CONCLUSION

In summary, we systematically investigate the electronic state of monolayer VSi_2N_4 and the spin-dependent transport properties of VSi_2N_4-based MTJs. We find that the state under 1.965% tensile strain is both a Weyl semimetal and a half-metal, with fully spin-polarized Weyl points around the Fermi energy that form a single spin channel. A large TMR of 1200% ratio and a perfect spin-injection efficiency are predicted in Ag/VSi_2N_4-VSi_2N_4/Ag MTJs. In particular, the TMR ratio can be increased by up to 10^5% by a compressive strain. The effects of biaxial strain and different tunnel barriers on the MTJ device are also included. We believe that our results will be helpful for the design and application of future two-dimensional spintronic devices.

FIG. 7. Benchmarking of TMR ratio and T_C in two-dimensional-magnetic-materials-based MTJ devices. MTJ devices based on Fe_3GeTe_2 and CrI_3 have been realized theoretically and experimentally.

[1] M. Julliere, Tunneling between ferromagnetic films, Phys. Lett. A **54**, 225 (1975).

[2] T. Miyazaki and N. Tezuka, Giant magnetic tunneling effect in Fe/Al$_2$O$_3$/Fe junction, J. Magn. Magn. Mater. **139**, L231 (1995).

[3] J. S. Moodera, Lisa R. Kinder, Terrilyn M. Wong, and R. Meservey, Large Magnetoresistance at Room Temperature in Ferromagnetic Thin Film Tunnel Junctions, Phys. Rev. Lett. **74**, 3273 (1995).

[4] Shinji Yuasa, Taro Nagahama, Akio Fukushima, Yoshishige Suzuki, and Koji Ando, Giant room-temperature magnetoresistance in single-crystal Fe/MgO/Fe magnetic tunnel junctions, Nat. Mater. **3**, 868 (2004).

[5] T. Marukame, T. Kasahara, K.-I. Matsuda, T. Uemura, and M. Yamamoto, High tunnel magnetoresistance in epitaxial Co/sub2/Cr/sub0.6/Fe/sub0.4/Al/MgO/CoFe tunnel junctions, IEEE. Trans. Magn. **41**, 2603 (2005).

[6] David D. Djayaprawira, Koji Tsunekawa, Motonobu Nagai, Hiroki Maehara, Shinji Yamagata, Naoki Watanabe, Shinji Yuasa, Yoshishige Suzuki, and Koji Ando, 230% room-temperature magnetoresistance in CoFeB/MgO/CoFeB magnetic tunnel junctions, Appl. Phys. Lett. **86**, 092502 (2005).

[7] S. Ikeda, J. Hayakawa, Y. Ashizawa, Y. M. Lee, K. Miura, H. Hasegawa, M. Tsunoda, F. Matsukura, and H. Ohno, Tunnel magnetoresistance of 604% at 300 K by suppression of Ta diffusion in CoFeB/MgO/CoFeB pseudo-spin-valves annealed at high temperature, Appl. Phys. Lett. **93**, 082508 (2008).

[8] Hemant Dixit, Vinayak Bharat Naik, Kazutaka Yamane, Taeyoung Lee, Jae-Hyun Kwon, Behtash Behin-Aein, Steven Soss, and William J. Taylor, in *2020 IEEE International Electron Devices Meeting (IEDM)* (IEEE, San Francisco, CA, 2020), p. 13.

[9] Cheng Gong, Lin Li, Zhenglu Li, Huiwen Ji, Alex Stern, Yang Xia, Ting Cao, Wei Bao, Chenzhe Wang, Yuan Wang, Z. Q. Qiu, R. J. Cava, Steven G. Louie, Jing Xia, and Xiang Zhang, Discovery of intrinsic ferromagnetism in two-dimensional van der Waals crystals, Nature **546**, 265 (2017).

[10] Bevin Huang, Genevieve Clark, Efrén Navarro-Moratalla, Dahlia R. Klein, Ran Cheng, Kyle L. Seyler, Ding Zhong, Emma Schmidgall, Michael A. McGuire, David H. Cobden, Wang Yao, Di Xiao, Pablo Jarillo-Herrero, and Xiondong Xu, Layer-dependent ferromagnetism in a van der Waals crystal down to the monolayer limit, Nature **546**, 270 (2017).

[11] Yujun Deng, Yijun Yu, Yichen Song, Jingzhao Zhang, Nai Zhou Wang, Zeyuan Sun, Yangfan Yi, Yi Zheng Wu, Shiwei Wu, Junyi Zhu, Jing Wang, Xianhui Chen, and Yuanbo Zhang, Gate-tunable room-temperature ferromagnetism in two-dimensional Fe$_3$GeTe$_2$, Nature **563**, 94 (2018).

[12] Tiancheng Song, Xinghan Cai, Matisse Wei-Yuan Tu, Xiaoou Zhang, Bevin Huang, Nathan P. Wilson, Kyle L. Seyler, Lin Zhu, Takashi Taniguchi, Kenji Watanabe, Michael A. McGuire, David H. Cobden, Di Xiao, Wang Yao, and Xiaodong Xu, Giant tunneling magnetoresistance in spin-filter van der Waals heterostructures, Science **360**, 1214 (2018).

[13] Xinlu Li, Jing-Tao Lu, Jia Zhang, Long You, and Yurong Su, Evgeny Y. Tsymbal, Spin-dependent transport in van der Waals magnetic tunnel junctions with Fe$_3$GeTe$_2$ electrodes, Nano Lett. **19**, 5133 (2019).

[14] Ce Hu, Dong Zhang, Faguang Yan, Yucai Li, Quanshan Lv, Wenkai Zhu, Zhongming Wei, Kai Chang, and Kaiyou Wang, From two- to multi-state vertical spin valves without spacer layer based on Fe$_3$GeTe$_2$ van der Waals homojunctions, Sci. Bull. **65**, 1072 (2020).

[15] Longfei Pan, Le Huang, Mianzeng Zhong, Xiang Wei Jiang, Hui Xiong Deng, Jingbo Li, Jian Bai Xia, and Zhongming Wei, Large tunneling magnetoresistance in magnetic tunneling junctions based on two-dimensional CrX$_3$ ($X =$ Br, I) monolayers, Nanoscale **10**, 22196 (2018).

[16] Wei Yang, Yuan Cao, Jiangchao Han, Xiaoyang Lin, Xinhe Wang, Guodong Wei, Chen Lv, Arnaud Bournel, and Weisheng Zhao, Spin-filter induced large magnetoresistance in 2D van der Waals magnetic tunnel junctions, Nanoscale **13**, 862 (2021).

[17] Tula R. Paudel and Evgeny Y. Tsymbal, Spin filtering in CrI$_3$ tunnel junctions, ACS Appl. Mater. Interfaces **11**, 15781 (2019).

[18] Dongzhe Li, Shuo Li, Chengyong Zhong, and Junjie He, Tuning magnetism at the two-dimensional limit a theoretical perspective, Nanoscale **13**, 19812 (2021).

[19] Zheng-Zhe Lin and Xi Chen, Ultrathin scattering spin filter and magnetic tunnel junction implemented by ferromagnetic 2D van der Waals material, Adv. Electron. Mater. **6**, 1900968 (2020).

[20] Xiaolei Ma, Jiezhi Chen, Kaiyou Wang, Runsheng Wang, and Ru Huang, in *2021 IEEE International Electron Devices Meeting (IEDM)* (IEEE, San Francisco, CA, 2021), p. 27.

[21] Yi-Lun Hong, Zhibo Liu, Lei Wang, Tianya Zhou, Wei Ma, Chuan Xu, Shun Feng, Long Chen, Mao-Lin Chen, Dong-Ming Sun, Xing-Qiu Chen, Hui-Ming Cheng, and Wencai Ren, Chemical vapor deposition of layered two-dimensional MoSi$_2$N$_4$ materials, Science **369**, 670 (2020).

[22] Kostya S. Novoselov, Discovery of 2D van der Waals layered MoSi$_2$N$_4$ family, Natl. Sci. Rev. **7**, 1842 (2020).

[23] Lei Wang, Yongpeng Shi, Mingfeng Liu, Ao Zhang, Yi-Lun Hong, Ronghan Li, Qiang Gao, Mingxing Chen, Wencai Ren, Hui-Ming Cheng, Yiyi Li, and Xing-Qiu Chen, Intercalated architecture of MA$_2$Z$_4$ family layered van der Waals materials with emerging topological, magnetic and superconducting properties, Nat. Commun. **12**, 1 (2021).

[24] Liemao Cao, Guanghui Zhou, Qianqian Wang, L. K. Ang, and Yee Sin Ang, Two-dimensional van der Waals electrical contact to monolayer MoSi$_2$N$_4$, Appl. Phys. Lett. **118**, 013106 (2021).

[25] Qirui Cui, Yingmei Zhu, Jinghua Liang, Ping Cui, and Hongxin Yang, Spin-valley coupling in a two-dimensional VSi$_2$N$_4$ monolayer, Phys. Rev. B **103**, 085421 (2021).

[26] Md Akanda, R Karim, and Roger K. Lake, Magnetic properties of NbSi$_2$N$_4$, VSi$_2$N$_4$, and VSi$_2$P$_4$ monolayers, Appl. Phys. Lett. **119**, 052402 (2021).

[27] Keshari Nandan, Barun Ghosh, Amit Agarwal, Somnath Bhowmick, and Yogesh S. Chauhan, An excellent 2D semiconductor for field-effect transistors, IEEE Trans. Electron Devices **69**, 406 (2021).

[28] Junsheng Huang, Ping Li, Xiaoxiong Ren, and Zhi-Xin Guo, Promising Properties of a Sub-5 nm Monolayer MoSi$_2$N$_4$ Transistor, Phys. Rev. Appl. **16,** 044022 (2021).

[29] Yulin Feng, Zilong Wang, Xi Zuo, and Guoying Gao, Electronic phase transition, spin filtering effect, and spin Seebeck effect in 2D high-spin-polarized VSi$_2$X$_4$ ($X =$ N, P, As), Appl. Phys. Lett. **120,** 092405 (2022).

[30] Qingyun Wu and Lay Kee Ang, Giant tunneling magnetoresistance in atomically thin VSi$_2$N$_4$/MoSi$_2$N$_4$/VSi$_2$N$_4$ magnetic tunnel junction, Appl. Phys. Lett. **120,** 022401 (2022).

[31] G. Kresse and J. Furthmüller, Efficient iterative schemes for ab initio total-energy calculations using a plane-wave basis set, Phys. Rev. B **54,** 11169 (1996).

[32] Søren Smidstrup, *et al.*, QuantumATK: An integrated platform of electronic and atomic-scale modelling tools, J. Phys.: Condens. Matter **32,** 015901 (2020).

[33] Jochen Heyd, Gustavo E. Scuseria, and Matthias Ernzerhof, Hybrid functionals based on a screened Coulomb potential, J. Chem. Phys. **118,** 8207 (2003).

[34] See Supplemental Material at http://link.aps.org/supplemental/10.1103/PhysRevApplied.19.014020 for more details of the computational results obtained in the present work, including electronic properties calculated by use of QuantumATK and VASP, band structures with and without

spin-orbit coupling, phonon band structures under different strains, and characteristics of devices based on other two-dimensional magnetic materials.

[35] Di Xiao, Gui-Bin Liu, Wanxiang Feng, Xiaodong Xu, and Wang Yao, Coupled Spin and Valley Physics in Monolayers of MoS$_2$ and Other Group-VI Dichalcogenides, Phys. Rev. Lett. **108,** 196802 (2012).

[36] Jing-Yang You, Cong Chen, Zhen Zhang, Xian-Lei Sheng, Shengyuan A. Yang, and Gang Su, Two-dimensional Weyl half-semimetal and tunable quantum anomalous Hall effect, Phys. Rev. B **100,** 064408 (2019).

[37] G. Schmidt, D. Ferrand, L. W. Molenkamp, A. T. Filip, and B. J. van Wees, Fundamental obstacle for electrical spin injection from a ferromagnetic metal into a diffusive semiconductor, Phys. Rev. B **62,** R4790 (2000).

[38] E. I. Rashba, Theory of electrical spin injection: Tunnel contacts as a solution of the conductivity mismatch problem, Phys. Rev. B **62,** R16267 (2000).

[39] Zhenhua Wu, F. M. Peeters, and Kai Chang, Electron tunneling through double magnetic barriers on the surface of a topological insulator, Phys. Rev. B **82,** 115211 (2010).

[40] Mika Oksanen, Andreas Uppstu, Antti Laitinen, Daniel J. Cox, Monica F. Craciun, Saverio Russo, Ari Harju, and Pertti Hakonen, Single-mode and multimode Fabry-Pérot interference in suspended graphene, Phys. Rev. B **89,** 121414 (2014).